

# Geometry and scaling of tangled vortex lines in three-dimensional random wave fields

A J Taylor and M R Dennis

H H Wills Physics Laboratory, University of Bristol, Tyndall Avenue, Bristol, BS8 1TL, UK

E-mail: alexander.taylor@bristol.ac.uk, mark.dennis@bristol.ac.uk

**Abstract.** The short- and long-scale behaviour of tangled wave vortices (nodal lines) in random three-dimensional wave fields is studied via computer experiment. The zero lines are tracked in numerical simulations of periodic superpositions of three-dimensional complex plane waves. The probability distribution of local geometric quantities such as curvature and torsion are compared to previous analytical and new Monte Carlo results from the isotropic Gaussian random wave model. We further examine the scaling and self-similarity of tangled wave vortex lines individually and in the bulk, drawing comparisons with other physical systems of tangled filaments.

PACS numbers: 02.40.Hw, 03.65.Vf, 05.40.-a

## 1. Introduction

Tangles of filaments filling 3-dimensional space occur generically in physics. In the theory of complex-valued scalar waves, such tangles occur as the *wave vortices* (also called nodal lines, phase vortices or wave dislocations) [1, 2] in linear superpositions of complex waves whose directions and phases are uniformly random but whose wavelength  $\lambda$  is fixed. Informally, these tangles of nodal filaments exist in any monochromatic component of 3-dimensional (3D) noise: in the light [3] or sound field in the space around us, or in an evolving and interfering matter wave without any overall direction of propagation. As such, these isotropic random wave fields are the most natural model of wave chaos [4], and lead to tangles of random vortices in models of chaotic 3D cavity modes [5]. These tangles are similar to initial conditions for models of cosmic strings [6], and isotropic, fully developed optical speckle patterns [7]. As they are nodal lines, no energy is associated with wave vortices, so their geometry and physics is distinct from other well-studied filamentary physical systems such as elastic rods, superfluid vortices, or defects in ordered media, despite the fact that all these systems form morphologically similar tangles. In this paper we investigate the small- and large-scale geometric structure of tangled wave vortices from computer simulations of random wave fields.

Although the geometric structure of tangled nodal lines in random wave superpositions is hard to characterise rigorously, several previous attempts have been made to approach them using analytic and numerical methods. On small lengthscales ( $\lesssim \lambda$ ) the amplitude of a chaotic random wavefield is a smooth complex function of position, so the nodal lines, as complex zero level sets, are themselves smooth space curves. Statistical quantities such as the density of vortex lines per unit volume [6, 8, 9] and the probability distribution of the vortex lines' curvature [8] can be computed analytically, treating the wave field as an isotropic Gaussian random function. Calculation of the statistical distribution of other geometric quantities, such as the lines' torsion, seems analytically intractable by these methods [10].

At larger lengthscales, properties of interest cannot be found analytically from differential geometry and the Gaussian random model, and computer experiments are necessary. Computer simulations of the nodal structure of random optical fields inside periodic 3D cells have indicated that, at distances much larger than the coherence length (comparable to  $\lambda$ ), a typical random nodal line looks like a Brownian random walk [7].

Our aim here is to explore, using large-scale computer simulations of random solutions of the Helmholtz equation in large periodic 3D cells, the crossover in the geometric behaviour of the tangle of vortices between the local regime where the vortices are smooth space curves, and longer lengths where the lines and tangles display various measures of statistical self-similarity. Our simulations employ superpositions of random waves with periodic boundary conditions, where the vortex tangle is periodic with a cubic fundamental cell (Figure 1), which are good approximations of wavefields whose statistics are genuinely statistically invariant to rotation.

More quantitatively, the wave fields we study are drawn from the ensemble of superpositions of complex-valued plane waves with random amplitudes and directions, i.e.

$$\psi(\mathbf{r}) = \sum_{\mathbf{k}} a_{\mathbf{k}} \exp(i\mathbf{k} \cdot \mathbf{r}) , \quad (1)$$

where  $\mathbf{r} = (x, y, z)$ , the wavevectors  $\mathbf{k}$  have the same fixed wavenumber  $|\mathbf{k}| \equiv k = 2\pi/\lambda$  so  $\psi$  in (1) satisfies the 3D Helmholtz equation  $\nabla^2\psi + k^2\psi = 0$ , and the complex amplitudes  $a_{\mathbf{k}}$  are independent, identically distributed circular Gaussian random variables. In our simulations, the  $\mathbf{k}$  are chosen to ensure cubic periodicity of the nodal pattern in real space; we impose that each  $\mathbf{k} = 2\pi\mathbf{c}/N$  for a fixed integer  $N$ , with  $\mathbf{c}$  a 3-vector of odd integers such that  $|\mathbf{c}| = \sqrt{3}N$ . Thus,  $\psi(\mathbf{r}) = \pm\psi(\mathbf{r} + \mathbf{d}N/2)$  for any  $\mathbf{d}$  in  $\mathbb{Z}^3$ , implying the zero pattern is periodic over half the period of the wavefield in each of the three periodic direction of the cell (i.e. one octant of a field cell). It is this periodicity of a cubic nodal line cell to which we refer through throughout the paper.

It is possible that the restriction on wavevectors to enforce Cartesian periodicity will affect some statistics of the field, such as the density of vortices or the scaling and fractal measurements of Section 4. We require periodicity instead for practical reasons; a non-periodic simulation would detect many line segments that exit through the boundaries rather than closing, severely limiting any investigation of large scale fractality or some

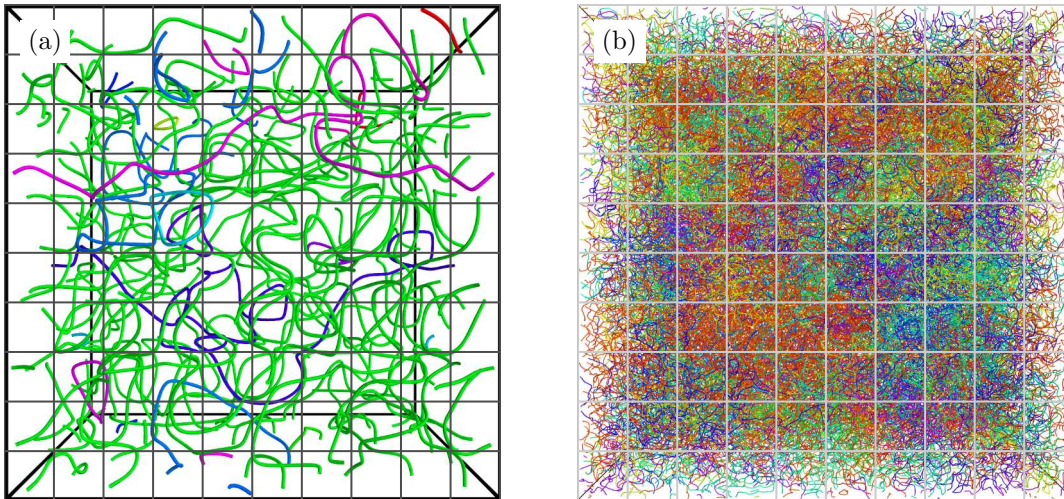


**Figure 1.** Examples of vortex tangles of random wave superpositions in periodic cells. Cells have side length (a)  $4.33\lambda$  and (b)  $21.7\lambda$ . Each unique vortex line is coloured differently. The grid lines are spaced at  $25\times$  the basic numerical sampling resolution (grid spacings of (a)  $0.43\lambda$  and (b)  $2.17\lambda$ ). As described in Section 2, the real numerical sampling resolution of (a) is at least 140 points per wavelength.

loop statistics. Directly resolving this problem demands impractically large simulation cells, or a different class of techniques to track individual vortex lines through a large volume, not knowing if or when the line will close and making it difficult to properly sample from loops of different lengths. In contrast, all loops in a periodic volume must close within it (with nuances discussed in Section 4), but this does not seem to significantly affect the known analytic statistics we investigate, as confirmed below.

Varying  $N$  whilst keeping  $\lambda$  fixed may be considered as changing the size of the periodic cell at fixed energy, making the vortex structure in cells of different sizes directly comparable. Equation (1) denotes a mathematically natural physical system, and in the limit  $N \rightarrow \infty$  is determined by only one physical length parameter—the wavelength  $\lambda$ —and so the geometric properties of the nodal lines of  $\psi(\mathbf{r})$  are purely inherent features of isotropic random wave interference.

The standard basis for locating the passage of vortices in complex scalar fields is the complex 2-dimensional  $\delta$ -function  $\delta^2(\psi)$ . Locating vortices as points in a 2-dimensional plane (say the  $xy$ -plane),  $\delta^2(\psi)$  counts one vortex when multiplied by the Jacobian  $\frac{1}{2}|\partial_x\psi^*\partial_y\psi - \partial_y\psi^*\partial_x\psi|$  (the sign of this purely imaginary quantity giving the 2D “charge”, that is, the sense of the circulation in  $x, y$ ). In three dimensions, this Jacobian generalizes to the *vorticity vector*  $\boldsymbol{\omega} \equiv \frac{1}{2}\text{Im}\nabla\psi^* \times \nabla\psi$  [8], a real vector directed along the vortex line tangent, given by the sense of circulation of phase around the vortex line, and  $\delta^2(\psi)|\boldsymbol{\omega}|$  gives the correct line length density of vortices in three dimensions [8]. We make use of this property in Section 3, but in our tracking of vortices in numerical cells we do not directly identify the zeros of the field or calculate  $\boldsymbol{\omega}$ . We instead observe the net phase change around every square plaquette in the cell: a vortex line pierces the

square plaquette (in the direction determined by the vorticity) when this phase change is  $+2\pi$  in an appropriate sense [7], and topological continuity of the discretized cells guarantees continuity of the vortex lines. In the limit of infinitely fine resolution, this should approach the theoretical curve defined by  $\delta^2(\psi)\omega$ .

Our simulations employ three distinct cell sizes, with side lengths  $4.3\lambda$ ,  $7.8\lambda$  and  $21.7\lambda$  (corresponding to  $N = 5, 9$ , and  $25$  respectively). Samples of the smallest and largest vortex cells are shown in Figure 1. In the mathematically ideal case, the cell would be infinitely large for fixed  $\lambda$ , and in the limit the sum would be over an isotropic, continuous distribution of wavevectors, captured analytically by the Gaussian random wave model (e.g. [8]). In practice the periodicity condition limits the sum to a smaller number of component wavevectors (effectively between 50 to 100; values of  $N$  are chosen to maximise these), which reduces statistical isotropy and may constrain some geometric quantities. A way this may be gauged is via the vortex densities in two and three dimensions, compared with their counterparts calculated analytically from the isotropic random wave model [8]: the ideal isotropic wave vortex tangle penetrates an arbitrary 2D plane at points with a density  $2\pi/3\lambda^2 \approx 2.09/\lambda^2$ , whilst in 3D the density of vortex *arclength* per unit volume is twice this,  $4\pi/3\lambda^2 \approx 4.19/\lambda^2$ . In our simulations with  $N = 25$ , the 2D density is  $(2.12 \pm 0.03)/\lambda^2$  in planes perpendicular to the axes of cubic periodicity, and  $(2.14 \pm 0.03)/\lambda^2$  through planes passing through the diagonal of a periodic cell face – both consistent with the theoretical result, and isotropic within the error bounds. The 3D vortex densities from simulation are  $(4.45 \pm 0.03)/\lambda^2$ ,  $(4.61 \pm 0.04)/\lambda^2$  and  $(4.49 \pm 0.03)/\lambda^2$  in cells with  $N = 5, 9, 25$  respectively, now not quite fully consistent with the theoretical result. We suspect this reflects the periodicity constraint, which forces vortex lines into loops more often than in the fully isotropic model (discussed further in Section 4), but does not appear significantly to affect our main results.

The properties of wave vortex tangles in this simple system will be compared with tangled filaments in other physical systems such as vortex filaments in turbulent superfluids, and polymer melts. They are also of interest by comparison with the high energy complex eigenfunctions of chaotic 3D cavities, for which functions of the form (1) are conjectured to be a good model, and for which the vortices in non-time-reversal-symmetric eigenfunctions [11] and resonances [12] have been studied in 2D. The wave vortices are the 3D nodal counterpart to the nodal lines bounding nodal domains in the 2D real chaotic case, whose behaviour has been extensively characterised [4, 13–16]. In particular, nodal line behaviour in the isotropic random wave model has been compared with numerically computed high-energy eigenfunctions in billiards. The results in this paper can be considered as some basic characterization of these nodal lines in 3 dimensions, including preliminary comparison between the isotropic model and complex eigenfunctions in the 3-torus (also see [17]). Physically, the vortex lines are important in wave chaos, for instance in dominating the flow of the current [5].

The structure of this paper is as follows. In the following Section, details are given of our numerical implementation of the random wave cells and the tracking of vortex lines

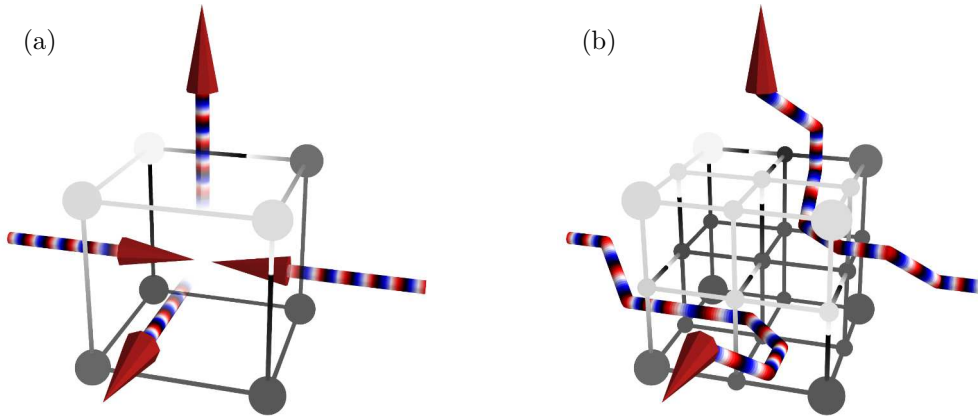


**Figure 2.** Demonstration of the supersampling vortex tracking algorithm. Each sphere at a vertex of the sampling grid represents a phase voxel, with phase indicated by greyscale. Lines between the voxels are coloured following a linear interpolation of phase between them (following the shortest change mod  $2\pi$ ). The patterned lines represent vortex lines, the increase red-white-blue denoting the direction of the vortex line, from a right-handed increase of phase. These lines enter or leave the cell through faces around which the total phase change is  $2\pi$ .

in them, especially the new supersampling technique we employ. In Section 3, we apply the numerical tracking on the short scale to extract the behaviour of curvature, torsion and their rate of change along a single vortex line, comparing with previous analytic results of curvature and new Monte Carlo (MC) calculations for torsion. Section 4 follows with an investigation of structure and scaling at larger scales, including the fractal behaviour of individual lines, the scaling of size and number of closed loops, and the fractal dimension of the tangle itself. We conclude with brief discussion.

## 2. Numerical random wave superpositions

In this Section we describe how the numerical tangle of vortex lines is extracted from the periodic random wave superpositions described above. The method follows previous numerical experiments [7], by sampling the field at points on a 3D cubic grid within the periodic cell, and searching for  $2\pi$  net phase changes around the four sides of each square plaquette face in the cubic lattice. (This is reminiscent of the so-called  $\mathbb{Z}_3$  lattice model in which the phases are themselves discrete [18].) Within each cube bounded by six such plaquettes, there may be a vortex denoted by a  $2\pi$  phase change oriented *into* the cube, and another vortex with a  $2\pi$  phase change oriented *out* of the cube. In this way the tangle of vortex lines can be built up through the volume. Readers uninterested in further details of vortex tracking may skip to Section 3.

The new feature of the tracking algorithm implemented here is that the basic sampling lattice is *resampled* in regions where the spatial details of the tangle are smaller

than the resolution of the sampling grid. This is important because the basic algorithm cannot resolve vortex topology when two or more vortex lines enter the same sampling grid cell, shown in Figure 2(a). In addition, the local vortex line geometry is poorly recovered unless the sampling grid resolution is high on the scale of the curvature of the line, but the computation time and memory requirements scale with the cube of the grid size. This ambiguity in resolving by vortex topology was approached in previous studies by different techniques; in the optical wave model of [7] using physical arguments, and in the discrete model of [18] by an extra random variable determining the topological assignment, or moving to a different 3D grid which does not permit ambiguity [19].

We believe our recursive resampling algorithm is more robust given the physics of our random wave model; whenever the local geometry or topology within a sampling cell cannot be resolved, the local phase structure in that cell is sampled again at a progressively higher spatial resolution until all local vortices can be fully distinguished, enforcing that no two vortex lines intersect the same cubic grid cell in the new resampled lattice.

Figure 2 shows an example of this process; the phase is initially sampled at the vertices of Figure 2(a) revealing only that two vortices enter and leave the cell through the four cell sides exhibiting a  $2\pi$  phase change. This is not enough information to distinguish the sub-cell topology of the vortices. After resampling, the paths of both vortex lines in Figure 2(b) are tracked without ambiguity, as they do not approach closely on the scale of the resampled grid. This fully solves the problems of both topological resolution and numerical efficiency by focusing computational effort on areas where vortices cannot be resolved properly, sampling only fairly sparsely elsewhere (say in volumes where there are no vortices).

This method resolves vortex lines very precisely on the sub-wavelength scale. However, the individual linear segments do not accurately reproduce the spatial conformation of the vortex filament, as it is assumed that each vortex line segment passes through the centre of the face where it are detected. The local fit is improved via three further numerical steps. First, once the vortex lines have been located, the resampling procedure is applied again to all the cells through which the vortex line passes, even if the topology is already well distinguished. This accurately traces the shape of the vortex curves without expending further numerical resources on the voids between longer vortices. In principle, extremely small vortex loops below the sampling cell may not be detected, but these are extremely rare and contribute a negligible amount to the total vortex arclength.

Secondly, rather than assuming the vortex line penetrates the centre of the grid face, we instead treat the face plane as a new, two-dimensional vortex location problem, and the intersection point is located by resampling the face with a 2D square grid of  $15\times$  the local 3D resampling resolution, and locating the square plaquette of this new grid around which there is still a  $2\pi$  phase change. The centres of these new plaquettes in the 2D face are joined by straight lines in the 3D grid to approximate the real vortex curve.

The result of these procedures is a representation of every vortex filament as a piecewise-linear space curve. Any remaining numerical noise and artefacts of the numerical sampling lattice are removed by downsampling this representation, keeping only every  $n$ th vertex, and fitting with a piecewise polynomial spline curve interpolation. In case the rigid sublattice sampling introduces high frequency noise to the fitting polynomial, the spline curve fit is required only to closely approximate the original vertices. We require that the sum of square distances between original and interpolated points does not exceed some small value;  $\sum_v (\mathbf{r}_v - \mathbf{r}_i)^2 < \delta L$ , where  $\mathbf{r}_v$  represents the vertices of the original piecewise linear curve,  $\mathbf{r}_i$  is the interpolated spline curve at each of these points,  $\delta$  is a fitting parameter,  $L$  is total length of the current vortex curve and the sum is over the vertices. This procedure resembles that of [20] in tracing superfluid vortices, though here we are concerned with accurately recovering the small scale geometry rather than removing noise on larger scales.

There are many possible choices of downsampling and interpolation parameters. We choose to downsample to every third vertex, and to set the fitting parameter  $\delta = 0.0001$ . These choices are such that the recovered geometry is stable to other values of each parameter.

Section 3 investigates local geometry which is sensitive to noise, and so results are taken largely from 2311 cells with  $N = 5$ , sampled with a high initial precision of  $0.0173\lambda$  ( $250^3$  sample points), and taking around 16 minutes on an average laptop using an optimised version of these algorithms via Python and Cython. At this resolution, around 0.19% of numerical grid cells contain a vortex segment, which must only rarely be resampled (in just  $\approx 0.15\%$  of these cases) due to the high initial resolution. A subsequent postprocessing stage re-resolves only the cells detected to contain vortices, at a resolution of  $0.00143\lambda$ , and taking  $\approx 2$  hours per numerical cell – this procedure would be impractical without a resampling algorithm focusing only on the pre-detected vortex curves. Further processing to remove numerical noise takes negligible time, and the resulting piecewise polynomials relate to the detected curves with at least 140 sample points per wavelength in order to accurately recover highly sensitive local geometry.

Section 4 investigates fractality over a wide range of scales in which the precise local geometry is not important, so these results are taken instead with 650 cells with  $N = 9$  and 47 cells with  $N = 25$  (e.g. Figure 1(b)), both sampled with an initial real space resolution of  $0.087\lambda$  ( $90^3$  and  $250^3$  points respectively). This takes around 80 seconds per cell with  $N = 9$  or 20 minutes with  $N = 25$ , and in both cases around 3.9% of grid cells contain vortices, with a further 4.6% of these being re-resolved to guarantee local continuity. The time scales mainly with the initial resolution of the sampling grid, though more time will be spent enforcing vortex continuity between cells if the initial sampling resolution is large on the wavelength scale, in which case vortices are often poorly resolved and must frequently be resampled to ensure an accurate trace. The results from these larger cells are not smoothed and resampled further than is necessary to resolve local topology, as our measurements of large scale fractality are not sensitive to small-scale numerical noise, and so the resulting piecewise linear curves have

resolution on the order  $0.087\lambda$  (excluding re-resolved regions), or just over 10 vertices per wavelength.

Following the above statistics, the basic computation time to topologically resolve vortices in an individual sample does not exceed 20 minutes (single threaded) for any of the individual numerical cells in our results. Memory requirements are also modest, and minor alterations to the algorithm could reduce them at the cost of a larger processing time.

### 3. Local geometry of single vortex curves

At the scale of a wavelength or less, we approach the geometric structure of the tangled melange of vortex filaments by considering the statistical shape of a single vortex line, ignoring the line's global topology and other lines nearby. At the scale of  $\lambda$ , the shape of the zero lines is limited by the Helmholtz equation, and the vortex lines are smooth space curves parametrised by *curvature*  $\kappa$  and *torsion*  $\tau$ , which, as functions of arclength  $s$  uniquely determine the shape of the curve [21], and are defined (as in Appendix A) in terms of derivatives along the curve with respect to  $s$ . As natural measures of the tangling of a single space curve,  $\kappa$  and  $\tau$  have been studied in other systems including superfluids [20] and even discrete lattice models [22]. We investigate the statistical distribution of these quantities via the isotropic Gaussian random wave model in which the probability distribution for curvature is available analytically [8], and the distributions of mathematically more complicated quantities can be obtained through Monte Carlo integration.

The curvature and torsion occur as part of the *Frenet-Serret* formalism of space curves, outlined in Appendix A. In our system, the arclength along wave vortex lines is naturally expressed in terms of the vorticity vector  $\boldsymbol{\omega} \equiv \frac{1}{2}\text{Im}\nabla\psi^* \times \nabla\psi$  (evaluated on nodal lines), whose direction gives the tangent to the vortex curve at that point (with respect to a right-handed increase of phase), leading to the expressions (evaluated on nodal lines)

$$\kappa = \frac{|\boldsymbol{\omega} \times (\boldsymbol{\omega} \cdot \nabla)\boldsymbol{\omega}|}{\omega^3}, \quad (2)$$

$$\tau = \frac{\boldsymbol{\omega} \times (\boldsymbol{\omega} \cdot \nabla)\boldsymbol{\omega} \cdot (\boldsymbol{\omega} \cdot \nabla)^2\boldsymbol{\omega}}{|\boldsymbol{\omega} \times (\boldsymbol{\omega} \cdot \nabla)\boldsymbol{\omega}|^2}. \quad (3)$$

The curvature therefore depends on second derivatives of the field, and the torsion on third derivatives. The numerator of  $\kappa$  occurs in the denominator of  $\tau$ , suggesting a statistical anticorrelation discussed further below.

Informally, the curvature and torsion of a space curve may be understood in terms of a local fit after a suitable translation and rotation to a *helix* of radius  $r$  and pitch  $c$ :  $\mathbf{a}(t) = (r \cos(t), r \sin(t), ct)$  (a helical vortex may be realised in a wave of the form of a perturbed screw dislocation [2, 10]). The curvature and torsion of the helix are the same at all points:  $\kappa = r/(r^2 + c^2)$  and  $\tau = c/(r^2 + c^2)$ . The local radius of curvature is  $1/\kappa > r$ ; in the limit  $c \rightarrow 0$ ,  $\kappa \rightarrow 1/r$  and the curve is locally a planar circular arc. In



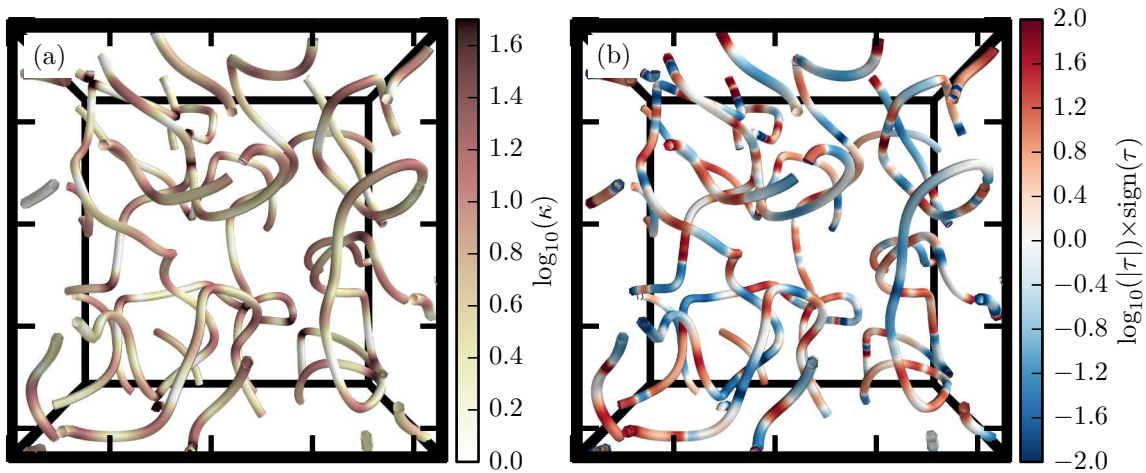


**Figure 3.** Curvature and torsion of a vortex tangle. Vortex lines are coloured by (a) curvature and (b) torsion, determined numerically. In each case, the same  $(2.17\lambda)^3$  volume of one of the cells described in Section 2 is shown, with the axis ticks marking  $0.5\lambda$  increments.

the opposite limit  $r \rightarrow 0$ , the helix becomes a straight line and  $\tau \rightarrow 1/c$ . This limit is therefore singular (the straight line has an arbitrary value of torsion, which is technically defined only when  $\kappa > 0$ ). This suggests that when, as here, physical considerations do not bound  $\tau$ , it can have very large fluctuations and is numerically ill-behaved when the curve is locally almost straight.

Figure 3 shows a simulated volume of vortex tangle, in which the vortex lines are coloured according to  $\kappa$  and  $\tau$ . Both quantities exhibit rapid changes on the sub-wavelength scale. By eye the curvature is usually small, but with localised regions of much higher curvature, particularly where pairs of vortex lines approach closely. The torsion is also often small with strongly concentrated regions, but these tend to occur in the less sharply curved segments of the vortex lines, indicating that the plane of curvature rotates about the vortex axis when the local curvature is small.

In other 3D systems with filamentary defect lines, the distributions of curvature and torsion have direct physical implications, relating to the local dynamics (as for superfluids [23]) or energetics (as for defects in liquid crystals [24]). In our case of linear wave superpositions, the wave vortices do not carry energy and are temporally static, and furthermore do not depend on the choice of any physical parameter except the wavelength.

### 3.1. Curvature

The curvature probability density function (PDF) for vortex lines in the continuum random wave model was found in [8] to have the Cauchy-like distribution

$$P(\kappa) = \frac{3^{5/2} \kappa \kappa_c^3}{(3\kappa_c^2 + \kappa^2)^{5/2}}, \quad (4)$$

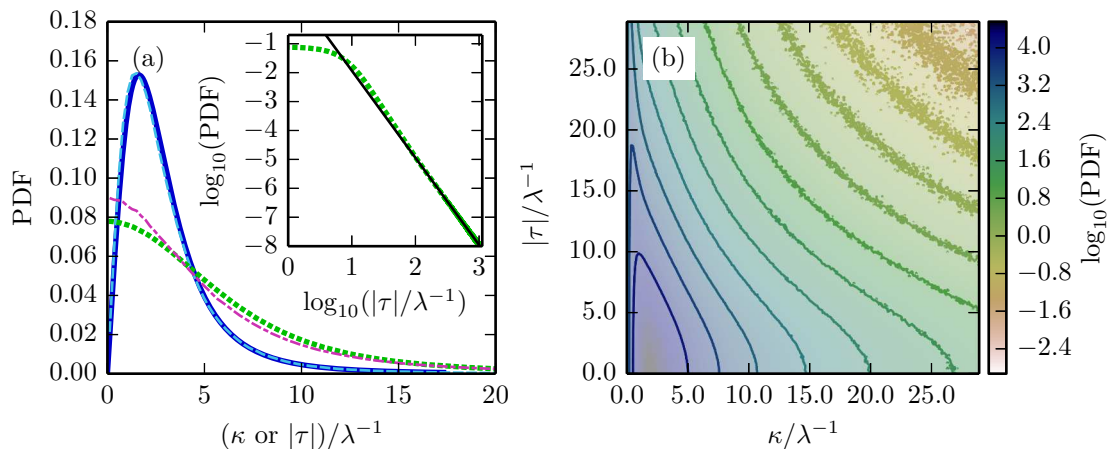


**Figure 4.** Curvature and torsion PDFs from the Gaussian random wave model and numerical simulations of random waves. (a) PDFs for curvature and torsion from simulations, analytic results and Monte Carlo integration; (b) joint PDF  $P(\kappa, \tau)$  drawn from Monte Carlo integration. In (a),  $P(\kappa)$  is determined by (4) (—), and from the random wave simulations (---). The torsion PDF is found by Monte Carlo integration (---) (described in Section 3.2), and in the simulations (---). Inset: Log-log plot indicating how  $\tau$  scales for larger values, as discussed in the text of Section 3.2. All Monte Carlo results come from  $6 \times 10^{10}$  points.

where, for fields satisfying the Helmholtz equation, the characteristic curvature  $\kappa_c = 4\pi/\sqrt{45}\lambda \approx 1.87/\lambda$ . Thus the peak of the distribution is at  $2\pi/\sqrt{15}\lambda \approx 1.62/\lambda$ , and its first two moments are

$$\langle \kappa \rangle = \sqrt{3}\kappa_c \approx 3.24/\lambda, \quad (5)$$

$$\langle \kappa^2 \rangle = 2\langle \kappa \rangle^2 = 6\kappa_c^2 \approx 21.1/\lambda^2, \quad (6)$$

whereas higher moments diverge. The values of these moments indicate that the lengthscales associated with vortex curvature are certainly sub-wavelength.

The curvature PDF extracted from our numerical simulations is shown in Figure 4. The agreement with (4) is very good, albeit with a slight discrepancy at small  $\kappa$  where the vortex tracing is imperfect and detail is lost by the linear piecewise approximation and smoothing. The peak of the recovered distribution is at  $\kappa = (2.71 \pm 0.05)/\lambda$ , a shift of 3.4%.

From the random wave simulations, we also recover the expectations and moments of the distribution

$$\langle \kappa \rangle = (3.18 \pm 0.06)/\lambda, \quad (7)$$

$$\langle \kappa^2 \rangle = (18.9 \pm 0.4)/\lambda^2 = 1.87\langle \kappa \rangle^2, \quad (8)$$

$$1/\sqrt{\langle \kappa^2 \rangle} = (0.230 \pm 0.002)\lambda. \quad (9)$$

These are comparable to the analytic results shifted to slightly lower curvatures, with the surprising exception that expected relationship  $\langle \kappa^2 \rangle = 2\langle \kappa \rangle^2$  is relatively strongly affected by the shift.

A fraction of the vortex line length in the simulation occurs as small loops (with size of around a wavelength or less), as anticipated in [25]. As these loops have curvature at least  $2\pi/\text{radius}$  over their length, they have uncharacteristically high curvature for the distribution. However, these loops account for only a small fraction of the overall vortex line length in the sample, and the PDF would be reproduced well even if only longer vortex lines were sampled.

### 3.2. Torsion

The torsion of a nodal line in a random wave field is less easy to interpret than its curvature. As can be seen in Figure 3,  $\tau$  varies rapidly over lengthscales comparable to or shorter than those of  $\kappa$  and, as discussed above, may be large even where a vortex filament is almost straight – it describes instead the local twisting of the Frenet frame about the tangent axis.

The statistical properties of the torsion of vortex lines have not explicitly been considered previously (except for brief comments in [8, 10]), as the form (3) of  $\tau$  is considerably more complicated than curvature  $\kappa$ : it depends on cubic combinations of fields and their derivatives (rather than quadratic combinations for curvature), which poses challenge for analytic evaluation by Gaussian techniques. Furthermore, the expression depends on first, second and third derivatives of field quantities, so the simplifications by symmetry and choice of coordinate system used in [8] cannot easily be applied, because third order derivatives are correlated with first order derivatives.

We instead consider the torsion PDF via Monte Carlo integration on the ensemble of the Gaussian model,

$$P(\tau) = \langle \tau(\mathbf{V}) \delta(\tau(\mathbf{V}) - \tau) P(\mathbf{V}) \rangle_{\mathbf{V}}, \quad (10)$$

where the average is the ‘dislocation average’ of [8], evaluated on vortex lines weighted probabilistically by arclength, and the vector of Gaussian random field quantities  $\mathbf{V}$  consists of all relevant field derivatives from (3). In the model these are each Gaussian distributed, and the probability  $P(\mathbf{V})$  includes all of their correlations and correctly-weighted variances. This PDF is shown in Figure 4.

The shape of the resulting numerical torsion PDF is distinctly different to that of the the curvature as it is a signed quantity, symmetric about  $\tau = 0$  (which is also therefore the peak of the distribution, and the ensemble is symmetric under  $\tau \rightarrow -\tau$ ). The first moment of the unsigned distribution is

$$\langle |\tau| \rangle = (6.19 \pm 0.09)/\lambda. \quad (11)$$

The torsion PDF decays much more slowly than that of the curvature, reflecting its quantitative instability when  $\kappa \approx 0$ . The high- $\tau$  scaling from the Monte Carlo integration is shown in the inset to Figure 4 (a), with linear fit  $\log P(\tau) = (-3.01 \pm 0.01)\tau$ , suggesting that as  $\tau \rightarrow \infty$ , the probability density scales as  $\tau^{-3}$ . We note that this behaviour occurs only when  $\tau \gg \lambda$ ; the fit becomes stable only for  $\tau \gtrsim 100/\lambda$ . If,

by analogy with  $\kappa_c$ , there is some characteristic torsion  $\tau_c$  determining the characteristic scaling of the distribution, then  $\tau_c \gg \kappa_c$ .

The  $\tau^{-3}$  scaling means that the second and higher moments of  $\tau$  diverge, as suggested in [10]. It is hard to identify by eye what the analytic form of  $P(\tau)$  might be; a range of PDFs with different analytic forms (including Cauchy-like distributions) occur as the distribution of various measures of vortex core twist and twirl [26]), but we have not been able to directly fit any of these families with *ad hoc* parameter choices to the Monte Carlo torsion distribution.

The torsion PDF recovered from our numerical experiments is shown in Figure 4 (for  $|\tau|$ ). The fit to the Monte Carlo result is again reasonable. The distribution from the simulations is shifted towards  $\tau = 0$ , similarly to the curvature; this shift is more pronounced here so the distribution is more significantly distorted from the Monte Carlo result. This reflects the numerical instability in measuring the torsion in our simulations; since the torsion may vary significantly even when the line is almost straight, it is highly sensitive to both numerical noise in the recovered curve and to our interpolation methods to remove this distortion (Section 2). In practice it is not feasible to recover the torsion PDF more accurately, though our result is stable to alternative choices of interpolation parameter.

The first moment of the recovered distribution is

$$\langle |\tau| \rangle = (6.00 \pm 0.06)/\lambda . \quad (12)$$

Unsurprisingly, the visual shift to low torsions translates to a lower moment, and the match to the Monte Carlo integral is less good than that of the curvature to the analytic result.

The Monte Carlo integration also makes accessible the joint curvature-torsion PDF, shown in Figure 4(b). It is consistent with the apparent distributions of Figure 3 and with the anticipated anticorrelation of  $\kappa$  and  $\tau$ . The curvature PDF is almost recovered on the symmetry line  $\tau = 0$ , with only a small shift in favour of higher curvatures.

As with curvature, the class of small vortex loops on the wavelength scale does not have a typical torsion distribution: as they have higher than average curvature, their torsion is correspondingly smaller, consistent with their being approximately planar as anticipated in [25].

### 3.3. Correlations of direction cosine, curvature and torsion

Although the probability density functions for curvature and torsion are consistent with what is seen by eye in Figure 3, they do not describe how curvature and torsion vary *along* the vortex line; we consider here some simple statistical lengthscales along the length of a vortex curve.

As we will discuss in more detail in Section 4, at long lengthscales vortex lines in random wave tangles approximate random walks. As is common in studies of Brownian random walks emerging from physical processes, we use the *persistence length*  $L_p$  is a natural scale for classifying long-scale behaviour [27]. It is defined from the

approximately exponential decay of the *direction cosine correlation* in random walks (i.e. correlation of tangent vectors  $\mathbf{T}(s)$  with respect to arclength  $s$ ), viz.

$$\langle \mathbf{T}(s) \cdot \mathbf{T}(s + \Delta s) \rangle \propto \exp(-\Delta s/L_p) , \quad (13)$$

where  $\mathbf{T}(s')$  is the tangent to the curve at the point labelled by  $s'$ , parametrised by arclength. As we will describe, the relevant  $\Delta s$  here is typically longer than any relevant lengths that can be extracted from the curve analytically by Taylor expansion (unlike curvature and torsion, which are derived at a single point via high derivatives).

This direction cosine correlation is plotted in Figure 5. As  $\Delta s \rightarrow 0$  the correlation function is determined by the mean square curvature through application of the Frenet-Serret relations (as in Appendix A),

$$\langle \mathbf{T}(s) \cdot \mathbf{T}(s + \Delta s) \rangle = 1 - \frac{1}{2} \langle \kappa^2 \rangle (\Delta s)^2 + O(\Delta s)^4 . \quad (14)$$

From Figure 5, this gives  $\langle \kappa \rangle = (3.2 \pm 0.1)/\lambda$ , consistent with the result of (7).

When  $\Delta s$  is larger, however, the correlation does *not* apparently have the simple exponential shape of (13), decaying instead less rapidly (Figure 5(a) inset). This is because the vortex space curve is still smooth (and not random) on the scale of wavelength: as  $\Delta s$  increases, the randomly varying curvature and torsion the curve's direction, but they do so with a more complicated distribution. The width of the function still gives an estimate for the correlation length scale; its second moment is  $(0.590 \pm 0.002)\lambda$ , and tangents become totally decorrelated over roughly the wavelength scale.

The varying of direction cosine with arclength along a vortex line can be compared directly that of the curvature and torsion, i.e. the correlation functions

$$C_\kappa(\Delta s) \equiv \frac{\langle \kappa(s) \kappa(s + \Delta s) \rangle}{\langle \kappa(s) \rangle^2} , \quad (15)$$

$$C_\tau(\Delta s) \equiv \frac{\langle \tau(s) \tau(s + \Delta s) \rangle}{\langle |\tau(s)| \rangle^2} . \quad (16)$$

These are shown in Figure 5(a). The curvature correlation is well-behaved, with vertical intercept matching (8). The torsion is noisier, and diverges as  $\Delta s \rightarrow 0$ .

The decay lengths of (15) and (16) give an indication of the length of vortex segment over which curvature and torsion become decorrelated. Both decay over a distance much shorter than a wavelength; in the case of the curvature, the second moment of  $(0.055 \pm 0.001)\lambda$  sets a rough lengthscale of correlation. Since the torsion correlation diverges, we instead fit its shape beyond  $\Delta s = 0.1$  to an exponential with decay length  $(0.24 \pm 0.03)\lambda$ .

An alternative measure of the torsion correlation distance comes from the *unsigned* torsion correlation, with  $\tau$  replaced by  $|\tau|$  in (16), also shown in Figure 5(a). As with the torsion, it diverges as  $\Delta(s) \rightarrow 0$ , but beyond  $\Delta(s) \cong 0.04\lambda$  it fits well to an exponential with decay length  $(0.08 \pm 0.01)\lambda$ . This sets a correlation lengthscale for torsion similar to that of the curvature.

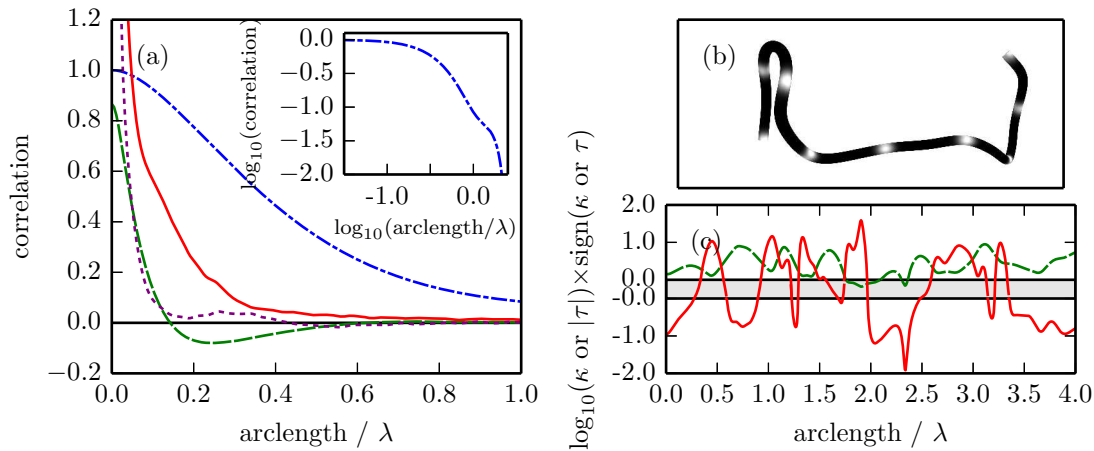


**Figure 5.** Variation of direction cosine, curvature and torsion with respect to arclength  $s$  along random vortex lines. (a) Correlation functions: direction cosine (13) (—), curvature correlation-1 (15) (---), signed torsion correlation (16) (—) and unsigned torsion correlation-1 (17) (---). (b) shows a typical short vortex segment taken from our numerical experiments, coloured with a white dot at every  $0.5\lambda$  arclength distance. (c) shows the varying curvature and torsion along the segment of (b). The scale of (c) is the signed logarithm  $\log_{10}(\kappa \text{ or } |\tau|) \times \text{sign}(\kappa \text{ or } \tau)$ , except in the shaded area which tracks the raw  $\kappa$  or  $\tau$  between  $\pm 1/\lambda$ .

These correlation curves and their associated lengthscales describe different features of the random filament, as in Figure 3. The persistence length quantifies the arclength interval of approximately fixed tangent direction along the curve as it undulates; this is the length along which a typical vortex line is (almost) straight. In between these sections are shorter intervals, whose length is the curvature correlation length, at which this direction changes rapidly. There are other even shorter intervals of high torsion (often when the curve is nearly straight) where the plane of curvature varies rapidly.

Figure 5(b-c) show a segment of a vortex curve randomly sampled from our numerical experiments, along with the curvature and torsion along its length, demonstrating how the correlation functions are expressed. Both exhibit small scale peaks, with widths following the correlation lengths above. These peaks are often strongly related to regions of hyperbolic interchange where two vortices approach closely, the hyperbolic analogues of the elliptic small loops previously mentioned to occur at small scales [25, 28, 29]. As with the loops, the smoothness of the field demands that these regions be highly curved but almost planar.

#### 4. Long-range scaling and self-similarity of vortex tangle

In the previous Section, we considered the geometry of individual vortex lines in random waves at a scale of a wavelength or less, and found good agreement at this local level between our numerical experiments of random waves in periodic 3D cells and the

isotropic Gaussian random wave model. However, such an approach cannot be directly extended to describe the geometry of the vortex tangle at scales beyond the wavelength – local methods, based on Taylor expansion, require too many terms to determine what quantities should be calculated, and even the probability distribution of torsion could not be calculated analytically. Following the approach of [7] in studying random 3D speckle fields satisfying the 2+1 Schrödinger equation (paraxial equation), we instead investigate the statistical self-similarity of the random vortex curves, and of the tangle: are they *fractal*, what are their statistics, and how do these compare with other models at the large scale?

Scaling and fractality has been well investigated in other models involving tangles of random filaments. In [18], it is shown that discrete  $\mathbb{Z}_3$  phase vortices in a cubic lattice model (as a certain simple caricature of cosmic strings in the early universe) behave as Brownian random walks, and observe that the assumption of a scaling continuum across longer lengthscales requires a certain distribution of long loop lengths. Similar results are found for vortex tangles in random optical waves (solving the 2+1 Schrödinger equation) [7], including Brownian fractal scaling in the radius of gyration of vortex loops [30]. It is also possible to determine the box-counting fractal dimension of the full vortex tangle, as performed for simulations of evolving superfluid turbulence [31], itself an extension of calculations for vortices in a classically turbulent field [32]. We compare all of these quantities within our own random wave model simulations (i.e. random solutions of the 3D Helmholtz equation whose periodic vortex cells are cubes), verifying that the fractal scalings of our vortices at long lengthscales are consistent with those in the 3D optical simulations [7]. These results are thus the 3D counterparts to the numerous random walk and percolation properties discussed for nodal lines in real 2D random waves as a model for quantum chaos [14].

Since the total vortex line length per simulated cell is finite, individual filaments are always closed, but may wrap around the periodic boundaries one or more times before closing. If the periodic cells are imagined as tiling infinite 3D space, such lines, on unwrapping, are infinite and periodic; when considered in the 3-torus, they have nontrivial homology. Other lines which do not wrap are simple loops, although they may span many cells. Taking a single period as the total arclength of a line, the total length of individual vortex lines varies from less than a wavelength in the smallest loops to the longest lines whose length is of comparable to the total arclength in the cell. These longest lines span many cells, having lengths of over  $40000\lambda$  in periodic volumes with side length just  $21.7\lambda$ .

The self-similarity of a single vortex curve can be determined by comparing, for one point on the curve fixed and the other varying along the curve, the arclength  $s$  between the pairs of points to the (unwrapped) Pythagorean straight line distance  $R$  [7, 18],

$$\langle R \rangle \sim C s^n, \quad (17)$$

where  $C$  is a constant and  $n^{-1}$  is the fractal dimension of the line:  $n = 1$  for a smooth line,  $n = 1/2$  for a Brownian random walk, and  $n \approx 0.588$  for a self-avoiding random

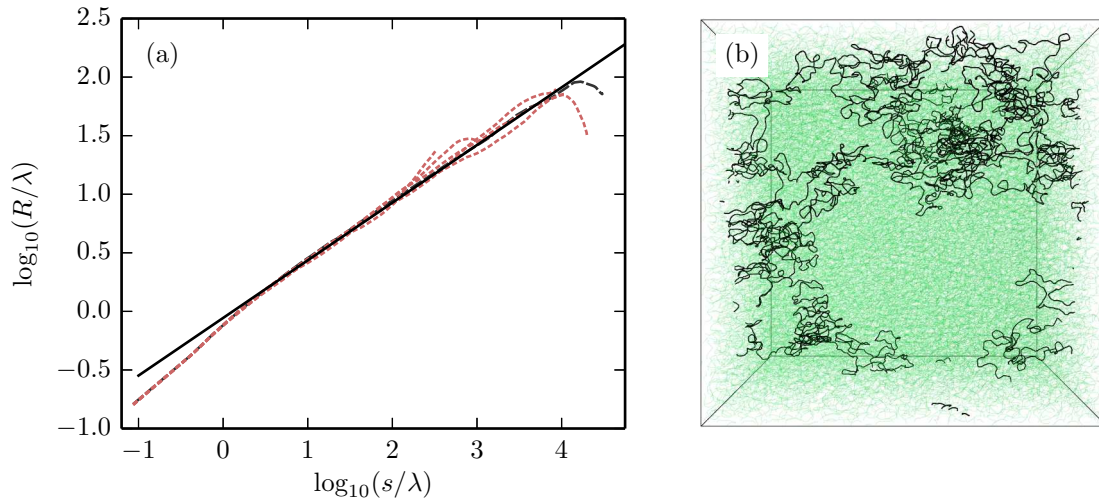


**Figure 6.** The scaling of straight line distance between vortex points against the arclength distance between them. (a) the log of the straight line distance  $R$ , averaged over 1500 pairs of points on the vortex curve separated by arclength  $s$ , against  $\log_{10}(s)$ . Between  $0.5 \leq \log_{10}(s) \leq 1.3$  the curves are fit to the same straight line (—) arising as the average gradient from 3000 individual curves, shown as the continuous black line with gradient  $0.504 \pm 0.002$ . Also shown are 5 examples of these curves (---), alongside a single much longer curve (—) almost three orders of magnitude longer than the fitted region but with the same fractal scaling persisting at larger scales. In (b), a sample periodic line of length  $401\lambda$  (in the middle of the length distribution), wrapped within its periodic cell, with several other lines and hundreds of loops (green).

walk [33]. The range at which (17) applies should be larger than the persistence length of the curve (it is smooth at smaller distances), and less than the overall length  $L$  of the curve (beyond which it repeats, either as a loop or a periodic line).

Figure 6 shows this scaling for our simulated vortex filaments from the larger cells averaging the Pythagorean distance  $R$  over 1500 pairs of points on each curve for each arclength separation  $s$ , giving a characteristic scaling relationship for each curve.

To limit contamination from (periodic) boundary effects, we consider a range of  $R$  constrained by the cell size  $0.5 \leq s \lesssim 21.7\lambda$ , and averaging over 3000 curves with a range of overall lengths (such as the sample in Figure 6(b)), we find  $n = 0.504 \pm 0.002$ . This is indicative of Brownian fractality, similar to the results of [7]. The lower limit for the Brownian scaling is around  $s \approx 3.5\lambda$  (somewhat higher than the persistence length  $L_p = 0.590\lambda$  described above), indicating that even when  $s > L_p$ , the smoothness of the field affects the line's statistical self-similarity. The scaling at lower arclengths is  $n \approx 0.63 \pm 0.02$ , although it is not clear what determines this exponent; our sampling resolution does not permit a resolution lower than about  $0.1\lambda$ .

We also fit 10 of the longest lines over their full length, not just within the span of a single cell; these vortex curves have lengths of at least  $10^4\lambda$ . The exponent for these lines is  $n = 0.493 \pm 0.03$  over three decades (and over a range significantly longer than the side length of the cell), with a single example shown in Figure 6(a). This



scaling behaviour continues the initial trend and appears highly typical, limited only by the size of the periodic cell. The characteristic hooked shape at the longest scales is a consequence of the periodic boundary conditions and the fact that cells tend to contain only one such very long line. This may be understood heuristically as follows. Each periodic cell must have the same vortex flux entering and leaving opposite faces. This constrains the paths of infinite periodic lines; for every ‘loop’ through the periodic boundaries, the same line or a different one must make an equal but opposite loop for the total flux to sum to 0. A long, unwrapped periodic line cannot typically roam far from any reference point, as the other lines in the cell must counter its flux. Since the other lines are typically much shorter, the long line cannot venture far and instead behaves almost like a loop, typically returning to a cell near its starting point. This manifests as the observed hook shape, in a similar manner to the way a loop losing its fractality at arclengths approaching its overall length by being forced to close within a finite distance.

The fractal self-similarity of closed loops may also be determined by comparing the loop’s overall length  $L$  against its radius of gyration  $r_g$  (i.e. the root mean square distance of all points on the loop from its centroid). At the smallest scale, an analysis based on local Taylor expansion shows that small vortex loops typically resemble small puckered ellipses, whose radius of gyration scales linearly with length, i.e.  $r_g \propto L$  [25]. However, for longer loops to have the characteristics of Brownian walks we expect that  $r_g \propto L^{1/2}$ . A log-log plot of loop length against radius of gyration for simulated vortex loops is shown in Figure 7, clearly demonstrating these two regimes, again with a rather sharp transition at  $L \approx 3.5\lambda$ . These loops are taken from cells of side length  $7.8\lambda$ . The smaller size is numerically optimal for tracing vortices in many cells in parallel, necessary since the radius of gyration cannot be averaged across a single loop, so many data points are necessary to check the scaling.

The fit beyond  $L \approx 3.5\lambda$  has gradient  $0.52 \pm 0.01$ , consistent with the 0.5 expected for random walks, though there is wide variation for individual loops. Below the transition the fit is instead to a gradient of  $0.98 \pm 0.01$ , consistent with the scaling of simple ellipses. Figure 7(b-g) shows examples of randomly selected loops across all these scales; small loops such as (b) demonstrate the small scale ellipse shape required by the smoothness of the field, while approaching the gradient cutoff introduces higher order terms that disrupt this shape as in (c). Beyond the cutoff the loops become tangled, no longer limited by the local smoothness of the field.

As discussed in [18], a truly scale invariant distribution of curves must appear the statistically the same at any given lengthscale. For Brownian curves, this suggests the number density of curves  $N(L)$  of length  $L$  should scale with  $L$  according to [18, 30]

$$N \propto L^{-3/2}. \quad (18)$$

Figure 8 shows the corresponding scaling from our numerical experiments. Beyond a loop length of  $3.5\lambda$ ,  $N(L)$  decays as  $L^{-(1.447 \pm 0.003)}$ . This is not fully consistent with our expectation, which we believe to be mainly an artefact of periodicity; as with the

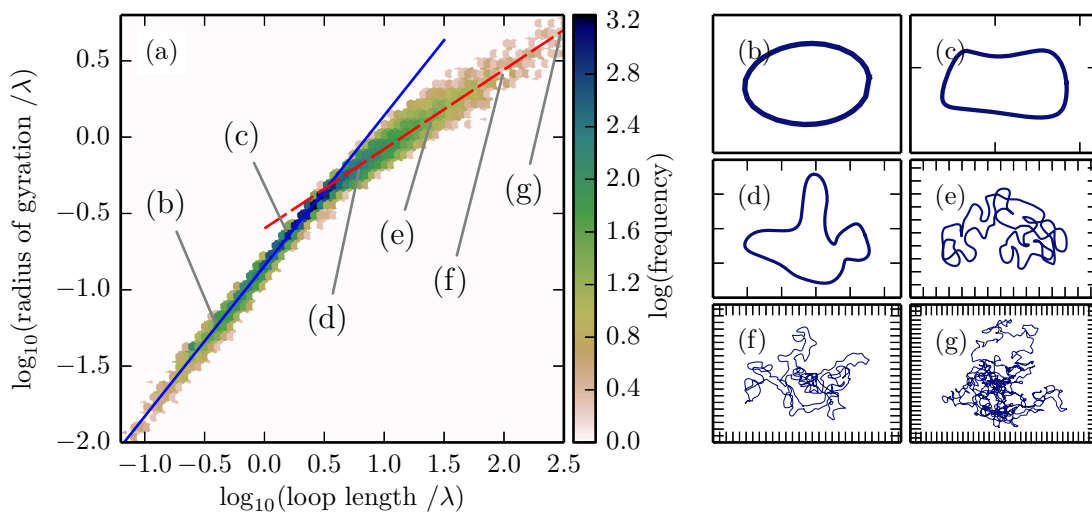


**Figure 7.** Scaling of random vortex loops. (a) Log-log plot of radius of gyration  $r_g$  against loop length  $L$ , for 39487 loops from 650 simulated cells of side length  $7.8\lambda$ . The fit for the lower values (—) has gradient  $0.98 \pm 0.01$ , while the fit for higher values (---) has gradient  $0.52 \pm 0.01$ , with the cutoff between regimes at  $(3.5 \pm 0.1)\lambda$ . (b-c) show examples of loops randomly selected at different length scales.

discussion of the numerical vortex density in Section 1, a difference between our periodic system and the ideal isotropic case is a requirement that lines close on relatively short scales, rendering the ideal continuum distribution of loops inaccessible. This same effect is responsible for the peak at maximal  $L$ ; in the continuum model, arbitrarily long loops would occur, but instead the periodicity constraint limits the total loop length to approximately the total arclength in a cell.

The preceding scaling measures apply to individual vortex curves. It is also possible to examine the self-similarity of the tangling *neighbourhood* of any point in the vortex field by means of the box counting dimension of the tangle [34]. This is obtained by tiling the cell with *boxes* of side length  $\delta$ , and considering the number of boxes  $N_b(\delta)$  containing a vortex line segment as a function of  $\delta$ . As above, we consider this in the range of large  $\delta$ , as the tangle is smooth in the range  $\delta \approx \lambda$ .

Following [32], the box counting fractal dimension  $n_b$  is defined as the scaling exponent in the expression

$$N_b(\delta) \propto \delta^{n_b} \quad (19)$$

over some range of  $\delta$  (which we expect to be larger than  $\lambda$ ); in the limit  $\delta \rightarrow 0$ ,  $N_b$  approaches the number of vortex sampling points; when  $\delta \lesssim \lambda$ ,  $n_b \approx 1$ , since the vortex tangle consists of lines. However, when  $\delta$  is very large (say the side length of the periodic vortex cell),  $N_b$  must simply equal 3 as every box will include at least one vortex segment. Any fractal region, if it exists, occurs between these two extremes.

$n_b$  is therefore a measure of the proportion of space (at a scale given by  $\delta$ ) which is filled by the curves. The box counting scaling for our numerical tangles is shown

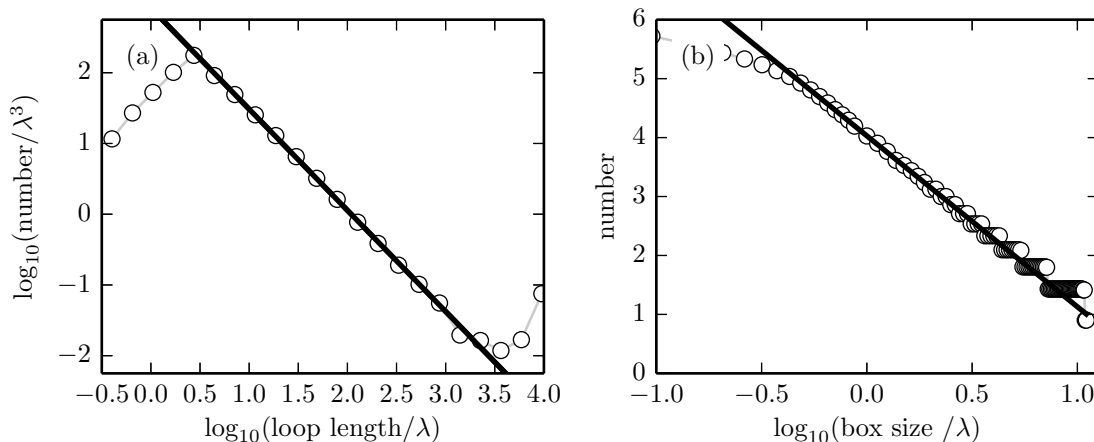


**Figure 8.** Scaling quantities for vortex curves. (a) Log-log plot of loop number (of fixed length) against the loop length, with a fit to gradient  $-1.447 \pm 0.003$ , from 1245899 loops in 4616 simulation cells with  $N = 9$ . (b) Deducing the box counting dimension of (19), with fit to the gradient  $2.90 \pm 0.01$ , averaging over 10 simulation cells with  $N = 25$ .

in Figure 8; the fit is to  $n_b = 2.90 \pm 0.01$  across a full decade of  $\delta$ : clearly  $n_b = 3$  indicates space is homogeneously filled at these scales. This space-filling regime in fact begins at around  $\delta \approx 0.6\lambda$ , well below the fractality scale of the other measurements and roughly on the scale of the persistence length. Thus the range in which the box-counting dimension is unity appears negligible.

In fact, this lower limit of  $0.6\lambda$  is close to the reciprocal square root density of points where vortex lines cross an arbitrary plane, of  $\sqrt{3/2\pi}\lambda \approx 0.69\lambda$ ; this is a measure of the mean spacing of vortex points. The fact that the space-filling regime begins at this scale seems to be an indicator of the previously discussed rigidity and regularity of random fields satisfying the Helmholtz equation [16, 35]. This property has been related in 2D to the infinite screening length of the vortex points as topological charges [8, 36]. Given that the screening length of distributions of wavenumbers (such as a Gaussian), we anticipate that vortices in these fields would display  $n_b = 3$  only at larger values of  $\delta$ .

Box counting fractality has also been investigated numerically in the vortex tangle of superfluid turbulence, where the scaling is directly affected by the dynamics of the flow and normal fluid interaction [31]. The fractal dimension depends on the vortex line density, but ranges only between 1.4 and 1.7 over a wide range of physical parameters. This is a strong contrast to vortices in random waves; although the vortex bulk is fractal, the lower dimension implies the line density is not distributed locally isotropically, instead surrounding vortex voids at all length scales. This is not evident in the self-similarity scaling of a single vortex, but is revealed when considering the scaling of the tangle as a whole.

## 5. Discussion

We have described various features of the random wave vortices/nodal lines in (almost-)isotropic superpositions of random waves satisfying the 3D Helmholtz equation, extracted mainly from numerical experiments in cubic 3D cells with periodic boundary conditions. Along a single vortex curve at scales of around a wavelength, we have seen that the probability distributions of curvature and torsion extracted from the simulations agrees well with the results of the isotropic Gaussian random wave model, and have identified numerically the different lengths of order  $\lambda$  at which various scalings occur. At larger length scales, we have verified that the tangle homogeneously fills space, but individual lines look like Brownian random walks and the distribution of closed loop lengths appears scale-invariant.

Many questions naturally arise from this numerical study. Most importantly, given the simplicity of this random wave model, might it be possible to derive any of these properties rigorously from the Helmholtz equation?

The geometric properties of vortex lines arise purely from interference, and the probability distributions of curvature and torsion are not difficult to extract (at least numerically) using the random wave model. Vortex lines in isotropic random functions with different power spectra were found to have similar properties to random Helmholtz waves in [8] (such as the same curvature distribution (4) but with different  $\kappa_c$ ); it is not clear whether similar PDFs lead to similar conformations of vortex lines, or whether they depend more subtly on correlations along vortex lines. According to the fundamental theorem of space curves, a curve's shape is determined uniquely by the curvature and torsion as functions of arclength. One might expect that the random walk behaviour arises from the vanishing of the various correlation functions along the vortex lines, but do these have additional subtle features which characterise them as random wave vortex curves? For instance, preliminary study of a different class of closed curves, specified by random finite Fourier series in Cartesian directions, look rather different to random vortex curves on visual inspection, yet have qualitatively similar curvature and torsion PDFs, and direction cosine, curvature and torsion correlation functions. Therefore, what geometric properties of random vortex lines characterise their geometry in particular?

Questions of the large scale *topology* of random vortex lines in the simulations are strongly affected by the periodic boundary conditions, in that most vortex length is in lines of nontrivial homology which wrap around the cell a nonzero number of times (which of course cannot occur in infinite cells). Such nontrivial homology lines appear to consume the majority of arclength in a given cell; in our cells with  $N = 9$ , they make up on average  $(83.1 \pm 0.2)\%$  of the total arclength in a cell, though this fraction varies widely between individual cells (it is not uncommon in fact for a cell only to contain lines of zero homology). This fraction is commensurate with 73% of lines in the optical model [30], or 81-86% in models of cosmic strings [18].

In fact, we find that each vortex cell typically contains one very long line of nontrivial homology, somewhat analogous to the existence of a percolating cluster in

regular percolation theory [37], and a small number of shorter ones. [38] suggests a Poisson-Dirichlet distribution for the distribution of line lengths is generic to a broad class of systems, but while this can exhibit the same characteristic mix of a single long and several short lines, it does not match the results reported here. As discussed in the main text, the total period length of the percolating line tends to be rather larger than the norm of its homology vector (i.e. the Pythagorean period length).

This local and long-range description characterises the tangled nodal forest in 3D complex, fixed-frequency noise. As such, the quantities we have described can be used as signatures for wave chaos in 3D complex billiard eigenfunctions or resonances, despite the fact that the PDFs, correlations and scaling laws do not appear to be particularly idiosyncratic to random wave vortex filaments rather than other patterns of tangles that occur in physics (or, indeed, other sorts of defect/singularity in other sorts of random wave field, such as polarisation singularities [1]). As described in [25, 29], features such as small loops and hyperbolic avoidances are determined by higher-order defects in the gradient of the complex scalar field (such as nodal lines of the complex scalar  $\nabla\psi \cdot \nabla\psi$ ), suggesting important features of the vortex tangle are in fact described by a hierarchy of tangled filaments describing the complex 3D morphology of the random field.

## Acknowledgments

We are grateful to S Whittington, M V Berry, J H Hannay and G P Alexander for discussions. This work was partially supported by NSF Grant No. PHY11-25915 under the 2012 KITP miniprogram “Knotted Fields.” AJT acknowledges financial support from the EPSRC.

## References

- [1] Dennis M R, O’Holleran K and Padgett M J 2009 Singular optics: optical vortices and polarization singularities *Progress in Optics* **53** 293–363
- [2] Nye J F and Berry M V 1974 Dislocations in wave trains *Proc. R. Soc. A* **336** 611–54
- [3] Freund I 2000 Optical vortex trajectories *Opt. Commun.* **181** 19–33
- [4] Berry M V 1977 Regular and irregular semiclassical wavefunctions *J. Phys. A: Math. Gen.* **10** 2083–91
- [5] Berggren K F and Ljung P 2009 Nature of streamlines for Berry-type wave functions in open 3D cavities *Mathematical modeling of wave phenomena (AIP Conference Proceedings vol 1106)* pp 253–59
- [6] Halperin I B 1981 Statistical mechanics of topological defects *Les Houches Session XXXV–Physics of Defects* ed Balian R, Kléman M and Poirier J P (North-Holland) pp 813–57

- [7] O'Holleran K, Dennis M R, Flossmann F and Padgett M J 2008 Fractality of light's darkness *Phys. Rev. Lett.* **100** 053902
- [8] Berry M V and Dennis M R 2000 Phase singularities in isotropic random waves *Proc. R. Soc. A* **456** 2059–79. Erratum **456** 3048.
- [9] Ishio H, Saichev A I, Sadreev A F and Berggren K F 2001 Wave function statistics for ballistic quantum transport through chaotic open billiards: statistical crossover and coexistence of regular and chaotic waves *Phys. Rev. E* **64** 056208
- [10] Dennis M R 2001 *Topological singularities in wave fields* Ph.D. thesis University of Bristol
- [11] Berry M V and Robnik M 1986 Quantum states without time-reversal symmetry: wavefront dislocations in a non-integrable Aharonov-Bohm billiard *Phil. Trans. R. Soc. A* **19** 1365–72
- [12] Höhmann R, Kuhl U, Stöckmann H J, Urbina J D and Dennis M R 2009 Density and correlation functions of vortex and saddle points in open billiard systems *Phys. Rev. E* **79** 016203
- [13] Blum G, Gnutzmann S and Smilansky U 2002 Nodal domains statistics - a criterion for quantum chaos *Phys. Rev. Lett.* **88** 114101
- [14] Bogomolny E and Schmit C 2002 Percolation model for nodal domains of chaotic wave functions *Phys. Rev. Lett.* **88** 114102
- [15] Monastra A G, Smilansky U and Gnutzmann S 2003 Avoided intersections of nodal lines *J. Phys. A: Math. Gen.* **36** 1845–53
- [16] Bogomolny E and Schmit C 2007 Random wave functions and percolation *J. Phys. A: Math. Gen.* **40** 14033
- [17] Gnutzmann S and Lois S 2014 Remarks on nodal volume statistics for regular and chaotic wave functions in various dimensions *Phil. Trans. R. Soc. A* **372**
- [18] Vachaspati T and Vilenkin A 1984 Formation and evolution of cosmic strings *Phys. Rev. D* **30** 2036–45
- [19] Hindmarsh M and Strobl K 1995 Statistical properties of strings *Nucl. Phys.* **B437** 471–88
- [20] Baggaley A W and Barenghi C F 2011 Spectrum of turbulent Kelvin-waves cascade in superfluid helium *Phys. Rev. E* **83** 134509
- [21] Gray A 1997 *Modern Differential Geometry of Curves and Surfaces with Mathematica* (CRC Press)
- [22] Bickis M G 1998 The torsion of three-dimensional random walk *Topology and geometry in polymer science* (Springer) pp 23–8
- [23] Kivotides D and Leonard A 2004 Geometrical physics of the many vortex filament problem *Europhys. Lett.* **66** 69–75
- [24] Kamien R D 2002 The geometry of soft materials: a primer *Rev. Mod. Phys.* **74** 953

- [25] Berry M V and Dennis M R 2007 Topological events on wave dislocation lines: birth and death of loops, and reconnection *J. Phys. A: Math. Gen.* **40** 65–74
- [26] Dennis M R 2004 Local phase structure of wave dislocation lines: twist and twirl *J. Opt. A: Pure Appl. Opt.* **6** S202–8
- [27] Orlandini E and Whittington S G 2007 Statistical topology of closed curves: some applications in polymer physics *Rev. Mod. Phys.* **79** 611–42
- [28] Nye J F 2004 Local solutions for the interaction of wave dislocations *J. Phys. A: Math. Gen.* **6** S251–4
- [29] Dennis M R, O’Holleran K and Padgett M J 2008 The fractal shape of speckled darkness *SPIE Proceedings* **6905** 69050C
- [30] O’Holleran K, Dennis M R and Padgett M J 2009 Topology of light’s darkness *Phys. Rev. Lett.* **102** 143902
- [31] Kivotides D, Barenghi C F and Samuels D C 2001 Fractal dimension of superfluid turbulence *Phys. Rev. Lett.* **87**
- [32] Vassilicos J C and Brasseur J G 1996 Self-similar spiral flow structure in low Reynolds number isotropic and decaying turbulence *Phys. Rev. E* **54** 467–85
- [33] Guillou J C L and Zinn-Justin J 1977 Critical exponents for the n-vector model in three dimensions from field theory *Phys. Rev. Lett.* **39** 95–8
- [34] Falconer K 1997 *Fractal Geometry: Mathematical Foundations and Applications* (John Wiley & Sons)
- [35] Foltin G, Gnutzmann S and Smilansky U 2004 The morphology of nodal lines: random waves versus percolation *J. Phys. A: Math. Gen.* **37** 11363–72
- [36] Kessler D A and Freund I 2008 Short- and long-range screening of optical phase singularities and C points *Opt. Commun.* **281** 4194–204
- [37] Stauffer D and Aharony A 1994 *Introduction to Percolation Theory* (CRC Press)
- [38] Nahum A, Chalker J T, Serna P, Ortuno M and Somoza A M 2013 Length distributions in loop soups *Phys. Rev. Lett.* **111** 100601

## Appendix A. Frenet-Serret Geometry

In our geometrical analysis, we consider vortices as one-dimensional space curves in three dimensions. Here we briefly review the details of the so-called Frenet-Serret formalism which describes the curvature, torsion and related quantities for a space curve in terms of its arclength parameter  $s$ , and how they relate to our physical model of wave vortex filaments. The following geometrical results about space curves are standard material, and can be found in textbooks such as [21].

We begin by assuming the curve is given by a vector function  $\boldsymbol{\gamma}(t)$ , where  $t$  is some arbitrary parameter which varies along the curve. Denoting derivatives with respect to  $t$  by  $\dot{\phantom{x}}$ , the  $t$ -derivative  $\dot{\boldsymbol{\gamma}}$  points in the direction of the (unit) tangent vector  $\boldsymbol{T}$

times a nonnegative quantity called the *velocity*  $v$ , i.e.  $\dot{\gamma} = v\mathbf{T}$ . In the case where the parametrization is the arclength,  $v = 1$ , and  $\frac{d}{ds}\gamma = \mathbf{T}$ .

The Frenet-Serret formalism follows simply from this fact. The derivative of the tangent with respect to the arclength,

$$\frac{d\mathbf{T}}{ds} = \kappa\mathbf{N}, \quad (\text{A.1})$$

defines the unit *normal* vector  $\mathbf{N}$  (which satisfies  $\mathbf{N} \cdot \mathbf{T} = 0$ ) and the nonnegative definite *curvature*  $\kappa$ , which determines the magnitude by which the tangent changes with arclength. A third vector, the *binormal*  $\mathbf{B} \equiv \mathbf{T} \times \mathbf{N}$ , completes an orthonormal basis at every regular point on the curve (i.e. where  $\kappa > 0$ ; this is true almost everywhere on vortex lines in random waves). Taking the derivative of  $\mathbf{N}$  with respect to arclength,

$$\frac{d}{ds}\mathbf{N} = \kappa\mathbf{T} + \tau\mathbf{B}, \quad (\text{A.2})$$

defining the *torsion*  $\tau$ , which can be positive (if the curve bends into the positive binormal direction) or negative (negative binormal). The shape of the curve is thus completely determined by the curvature and torsion as functions of arclength; this result is the *fundamental theorem of space curves*.

If the curve is specified by a parameter  $t$  which is not simply the arclength, the curvature and torsion can still be extracted from derivatives of  $\gamma$  with respect to  $t$  using the chain rule,

$$\ddot{\gamma} = v^2\kappa\mathbf{N} + \dot{v}\mathbf{T} \quad (\text{A.3})$$

$$\ddot{\gamma} = v^3\kappa\tau\mathbf{B} + (2v\dot{v}\kappa + v^2\dot{\kappa})\mathbf{N} + (v\dot{v} + \ddot{v})\mathbf{T}. \quad (\text{A.4})$$

Using the orthogonality properties of the vectors  $\mathbf{T}$ ,  $\mathbf{N}$  and  $\mathbf{B}$ , it is straightforward to show that

$$\kappa = \frac{|v\ddot{\gamma} - \dot{v}\dot{\gamma}|}{v^3} \quad (\text{A.5})$$

$$\tau = \frac{\dot{\gamma} \times \ddot{\gamma} \cdot \ddot{\gamma}}{|v\ddot{\gamma} - \dot{v}\dot{\gamma}|^2}, \quad (\text{A.6})$$

On a vortex curve, the vorticity vector  $\boldsymbol{\omega} \equiv \frac{1}{2} \text{Im } \nabla\psi^* \times \nabla\psi$ , which points along the vortex line, conveniently defines a parametrization of a vortex curve whose velocity is the modulus  $\omega = |\boldsymbol{\omega}|$ , and  $\boldsymbol{\omega} = \omega\mathbf{T}$ . Furthermore, derivatives with respect to this parametrization are represented by a convective-like derivative  $\boldsymbol{\omega} \cdot \nabla$ . Appropriate substitutions of  $\boldsymbol{\omega}$  and  $\boldsymbol{\omega} \cdot \nabla$  for  $\dot{\gamma}$  and  $d/dt$  in (A.5) and (A.6) give the expressions (2) and (3) used in the main text.